5-1-2019

First-Principles Study of FeO_2H_x Solid and Melt System at High Pressures: Implications for Ultralow-Velocity Zones

Jie Deng
Yale University

Bijaya B. Karki
Louisiana State University

Dipta B. Ghosh
Louisiana State University

Kanani K.M. Lee
Yale University

Recommended Citation

Deng, J., Karki, B., Ghosh, D., & Lee, K. (2019). First-Principles Study of FeO_2H_x Solid and Melt System at High Pressures: Implications for Ultralow-Velocity Zones. *Journal of Geophysical Research: Solid Earth, 124* (5), 4566-4575. https://doi.org/10.1029/2019JB017376

JGR Solid Earth

RESEARCH ARTICLE
10.1029/2019JB017376

Key Points:
- Pyrite-type FeO_2H_x is likely to be melted near the core–mantle boundary
- The seismic velocity of liquid FeO_2H is much lower than pyrite-type FeO_2H solid
- A molten FeO_2H_x induced ultralow-velocity zone requires high viscosity and/or vigorous convection

Supporting Information:
- Supporting Information S1

Correspondence to:
J. Deng,
jie.deng@yale.edu

Citation:
Deng, J., Karki, B. B., Ghosh, D. B., & Lee, K. K. M. (2019). First-principles study of FeO_2H_x solid and melt system at high pressures: Implications for ultralow-velocity zones. *Journal of Geophysical Research: Solid Earth*, *124*, 4566–4575. https://doi.org/10.1029/2019JB017376

Received 15 JAN 2019
Accepted 18 APR 2019
Accepted article online 25 APR 2019
Published online 21 MAY 2019

First-Principles Study of FeO_2H_x Solid and Melt System at High Pressures: Implications for Ultralow-Velocity Zones

Jie Deng[1], Bijaya B. Karki[2], Dipta B. Ghosh[2], and Kanani K. M. Lee[1]

[1]Department of Geology and Geophysics, Yale University, New Haven, CT, USA, [2]School of Electrical Engineering and Computer Science, Department of Geology and Geophysics, and Center for Computation and Technology, Louisiana State University, Baton Rouge, LA, USA

Abstract Pyrite-type FeO_2H_x (P phase) has recently been suggested as a possible alternative to explain ultralow-velocity zones due to its low seismic velocity and high density. Here we report the results on the congruent melting temperature and melt properties of P phase at high pressures from first-principles molecular dynamics simulations. The results show that P phase would likely be melted near the core–mantle boundary. Liquid FeO_2H_x has smaller density and smaller bulk sound velocity compared to the isochemical P phase. As such, relatively small amounts of liquid FeO_2H_x could account for the observed seismic anomaly of ultralow-velocity zones. However, to maintain the liquid FeO_2H_x within the ultralow-velocity zones against compaction requires special physical conditions, such as relatively high viscosity of the solid matrix and/or vigorous convection of the overlying mantle.

Plain Language Summary Ultralow-velocity zones (ULVZs) are 5–40-km-thick patches lying above Earth's core–mantle boundary. They are characterized with anomalously low seismic velocities compared with the ambient mantle and may contain important clues on the thermochemical evolution of the Earth. A recent experimental study argued that ULVZs may be caused by the accumulation of pyrite-type FeO_2H_x (P phase) at the bottom of the mantle. Here for the first time, we systematically study the thermoelastic properties of both FeO_2H_x solid and liquid phases. We find that P phase is likely melted near the core–mantle boundary and thus cannot be the source of ULVZs. Furthermore, in order for the molten product of P phase to cause ULVZs, the dense and nearly inviscid melts must be dynamically stable and confined within the ULVZs, which requires that the mantle is highly viscous and/or convects vigorously.

1. Introduction

Ultralow-velocity zones (ULVZs) are 5–40-km-thick patches lying directly above the core–mantle boundary (CMB), where seismic wave speeds are depressed by ~10% for *P* waves and 10–30% for *S* waves (Williams & Garnero, 1996). Several mechanisms have been proposed to explain ULVZs, including the oft-cited partial melting (Williams & Garnero, 1996) and solid-state iron-enriched materials (Brown et al., 2015; Mao et al., 2006; Wicks et al., 2010). The different mechanisms correspond to distinctive thermal and chemical states of the CMB resulting from different Earth evolution scenarios. Careful assessment of the different proposed mechanisms including the compositional likelihood and stability field at such depths therefore becomes necessary to distinctively pinpoint the actual origin(s) of ULVZs.

Recently, pyrite-type FeO_2H_x (x = 0-1, named P phase hereafter) has been invoked as a plausible cause of ULVZs (Liu et al., 2017). Based on their laser-heated diamond-anvil cell experimental results, Liu et al. (2017) suggested that the pyrite-type iron peroxide with varying hydrogen concentration is stable up to 2,600 K and 133 GPa while exhibiting thermoelastic properties consistent with ULVZs. The temperature near the CMB is, however, generally expected to reach ~4,000 K at 136 GPa (Anderson, 2002). Under such extreme conditions, the stability of P phase remains unclear. The comparison with the melting behavior of FeO may shed light on this issue. The melting temperature of FeO at the CMB is around 3,700 K (Fischer & Campbell, 2010) and falls into the lower end of the proposed CMB temperature (Andrault et al., 2016; Nomura et al., 2014). The P phase contains more light elements and thus may be less refractory as the addition of hydrogen/oxygen usually tends to lower the melting temperatures of the system (e.g., Morard et al., 2017; Nomura et al., 2011). Therefore, P phase might melt at the lowermost mantle.

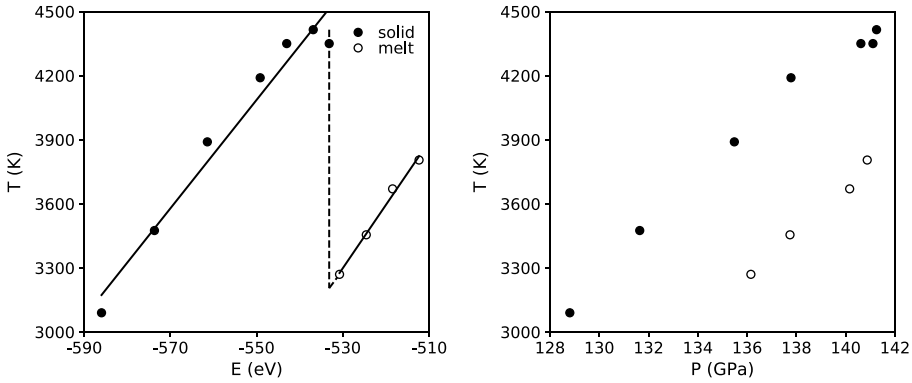

Figure 1. (a) The *Z* isochores in temperature-total energy and (b) temperature-pressure domains for pyrite-type FeO_2. The lower bound of the melting temperature (3,205 K) is taken as the temperature at which the total energy of the liquid equals the maximum total energy of the solid reached in the simulation (the intersection of the vertical dashed line and the liquid branch). The lowest temperature of the melt (3,275 K) is taken as the upper bound of the melting temperature.

If P phase melts near the CMB, the resulting melt may have very different seismic and dynamic properties. To assess the (solid/liquid) phase stability of FeO_2H_x composition at the CMB, we calculate the melting temperature of the two end-members of P phase, that is, FeO_2 and FeO_2H, from first-principles molecular dynamics (FPMD) simulations. Thereafter, we evaluate the thermoelastic properties of liquid FeO_2H_x and further examine whether it could be the source material for ULVZs.

2. Computational Methodology

Our FPMD simulations are based on density functional theory and projector augmented wave method as implemented by Vienna Ab initio Simulation Package (Blöchl et al., 1994; Kresse & Joubert, 1999). While we used the generalized gradient approximation (GGA) for the exchange-correlation functional (Perdew et al., 1996), we also explored the effects of the Hubbard term with $U = 5$ and $J = 0.8$ eV (Jang et al., 2017) and local density approximation (LDA). The plane wave cutoff was set at 400 eV (which resulted in Pulay stress of 6–10 GPa), and Brillouin zone sampling was performed at the Gamma point. The time step was set at 0.5 to 1 fs, and the allowed error in total energy was set between 10^{-4} and 10^{-6} eV. The run durations varied from 5 to 20 ps. The supercells contained $Fe_{32}O_{64}$, $Fe_{32}O_{64}H_{32}$, and $Fe_{16}O_{32}H_{80}$.

To calculate the melting temperatures of FeO_2H and FeO_2 at high pressures, we used the *Z* method, which is based on the notion that the internal energy of the crystal at the superheating limit equals that of the isochemical liquid at the melting temperature (Belonoshko et al., 2006). It has been previously used in multiple melting studies (Belonoshko & Rosengren, 2012; González-Cataldo et al., 2016; Li et al., 2014; Wang et al., 2013). We performed FPMD simulations in the microcanonical (*NVE*) ensemble on a single solid system at different initial energies controlled by the initial temperature set in each simulation. When the crystal is heated beyond its overheating limit, the temperature naturally drops to the melting temperature as the latent heat is removed from the kinetic energy. The connected *P*-*T* points on the isochore form a *Z*-shaped curve. Several simulations for each isochore are needed in order to yield a single accurate melting temperature (Figures 1 and S1). The *Z* method only works for congruent melting because it compares the internal energy variation of an isochemical solid and liquid. FeO_2 may melt congruently while FeO_2H may melt incongruently as discussed in detail in the following section. Nevertheless, the calculated "congruent melting temperature" of FeO_2H informs how the addition of hydrogen would affect the melting temperature of the FeO_2H_x system. To study the equation of state of FeO_2H_x solid and liquid, we then performed several FPMD simulations in the canonical (*NVT*) ensemble. We confirmed the physical state (solid or liquid) of the simulated system by examining the partial radial distribution functions (Figure S2) and atomic trajectories (Figure S3). We also found that running longer simulations (>20 ps) and doubling supercell ($Fe_{64}O_{128}$) did not affect the calculated results significantly; for instance, final pressure and temperature from our *NVE* runs varied by less than 0.2 GPa and 100 K, respectively.

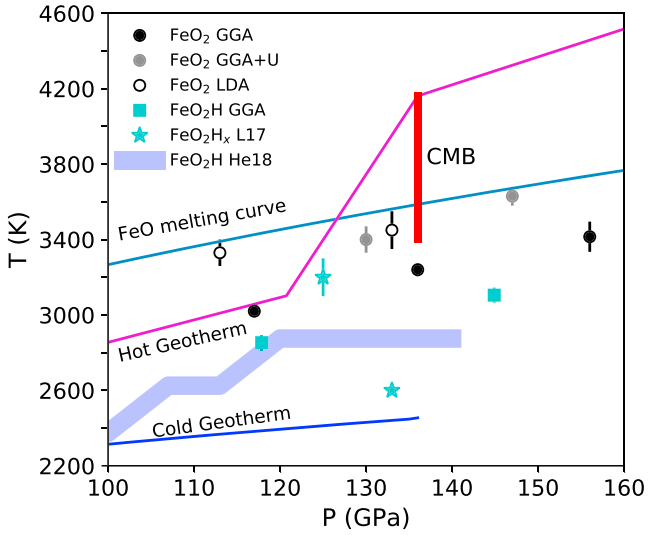

Figure 2. Congruent melting temperatures of FeO_2 (solid circles) and FeO_2H (solid squares) using GGA at high pressures (with the GGA+*U* and LDA results shown for FeO_2 by grey and open circles, respectively). Two high-temperature experimental data where P phase is observed are plotted as asterisks (Liu et al., 2017) and the FeO melting curve is taken from Fischer and Campbell (2010). The thick blue zigzag curve is the calculated phase boundary between solid and liquid FeO_2H from (He et al., 2018). Also shown are the cold geotherm (Brown & Shankland, 1981) and hot geotherm (Anderson, 2002). The vertical bar represents the range of literature values for the CMB temperature (Andrault et al., 2016; Nomura et al., 2014).

3. Results and Discussion

3.1. Melting Temperatures

The congruent melting temperatures of FeO_2 and FeO_2H were calculated near CMB pressures as summarized in Figure 2. For FeO_2, the melting temperature using GGA increases from 3,020 ± 30 K at 117 GPa to 3,415 ± 80 K at 156 GPa, in good agreement with the previous calculation (Zhang et al., 2017). For FeO_2H, the melting temperature using GGA is in agreement with He et al. (2018) at 118 GPa but not at higher pressures. Note that He et al. (2018) estimated the boundary between the melt/solid FeO_2H by simulating at widely spaced *P-T* conditions, which cause the zigzag melting boundary and the apparent discrepancy with our results. The calculated melting temperatures of FeO_2 are lower than the experimental FeO melting curve (Fischer & Campbell, 2010), as one would expect intuitively. Our results show that FeO_2H melts at lower temperatures at the pressures investigated, which implies that adding H into FeO_2 further lowers the melting temperature when compared to FeO. FeO_2 can be viewed as the binary mixing of FeO-O_2. Although the end-member O_2 is much less refractory than Fe, the melting temperature of the mixing product FeO_2 is very close to the eutectic melting temperature of Fe-FeO system (3,200 ± 200 K; Seagle et al., 2008; Morard et al., 2017). For the sake of comparison, we have also estimated the melting temperature both by GGA+*U* and LDA. The values are shifted upward by 200 to 300 K (Figure 2). To elaborate, because LDA tends to overbind, it results in higher melting temperature in comparison to GGA. Similarly, although no data on the effects of *U* on the melting temperatures exist, the penalty function *U* in GGA+*U* is known to increase the transition (structural and spin) pressures (Ghosh & Karki, 2016). Irrespective of the choice (i.e., LDA, GGA, or GGA+*U*), our results (Figure 2) suggest that FeO_2H_x systems are likely to be molten near the CMB.

The FPMD simulations put meaningful constraints on the melting temperature of P phase. We note that our predicted congruent melting temperature of P phase falls very close to one experimental data point (125 GPa, 3,100–3,300 K) which observed solid-state FeO_2H_x for x = 0.5–0.7 (Liu et al., 2017). There are a couple of possible reasons why P phase was observed at such high temperatures. First, large temperature gradients likely existed in LHDAC experiments, and as such, accurate temperature measurement is difficult (Deng et al., 2017) especially for flash heating. Second, if the kinetics of melting is slow, P phase may be metastable at temperatures higher than its melting temperature given the short flash heating durations.

Comparison between the melting temperatures of FeO_2 and FeO_2H with mantle geotherms together with high-pressure experiments (e.g., Liu et al., 2017; Yuan et al., 2018) suggests that P phase is thermally stable (not melted) in most of the mantle (Anderson, 1982, 2002; Brown & Shankland, 1981). However, this may not be the case in the lowermost mantle and within the thermal boundary layer right above the CMB where mantle temperatures drastically increase by 1,000–1,400 K within less than 200 km estimated from mantle adiabat and the melting temperature of core materials at CMB conditions (Anderson, 2002; Anzellini et al., 2013; Morard et al., 2017). The congruent melting curve of P phase likely intersects with the geotherm, indicating the onset of melting. The exact depth at which melting can occur depends on the hydrogen content and the mantle temperature profile. No matter where within the thermal boundary layer melting occurs, P phase is not thermally stable within the ULVZs that are characterized by CMB temperatures.

The above discussion is based on the assumption that P phase melts congruently. However, as mentioned earlier, P phase may not melt congruently. Nishi et al. (2017) argued that P phase would dissociate into post-perovskite type Fe_2O_3 and H_2O above 2,400 K at lowermost mantle pressures. This is in contrast to the experiments (Hu et al., 2017; Liu et al., 2017) where P phase is found to be stable at temperatures as high as 3,100–3,300 K (Figure 2). On the other hand, a recent first-principles study computed the Gibbs free

energies of the decomposition reaction of FeO_2 ($FeO_2 = Fe_2O_3 + O_2$) at 40 to 80 GPa and up to 2,400 K and found that this reaction is not energetically favorable at high pressures (>40 GPa; Tang et al., 2018), supporting the experimental observations by Hu et al. (2017) and Liu et al. (2017). Another static first-principles study suggested that at lowermost mantle conditions, the dehydrogenation dissociation ($FeO_2H = FeO_2H_x + \frac{(1-x)}{2}H_2$) of pyrite-type FeO_2H is energetically unfavorable while the dehydration dissociation ($2FeO_2H = Fe_2O_3 + H_2O$) may be energetically accessible, in agreement with Nishi et al. (2017).

If P phase (including FeO_2 and FeO_2H_x ($x > 0$)) melts incongruently, the incongruent melting products may be FeO_2H_x, FeO_2, Fe_2O_3, H_2O, H_2, and O_2 according to the discussion above. Unlike congruent melting, the melting temperature of P phase needs be further subdivided into the solidus melting temperature and the liquidus melting temperature, both of which are related to the end-member melting temperatures and mixing properties. Due to the lack of mixing parameters between end-members (FeO_2, Fe_2O_3, H_2O, H_2, and O_2) at CMB conditions, we consider only ideal mixing. In this case, the solidus and liquidus melting temperatures of P phase range from the lowest melting temperatures to the highest melting temperatures of the end-members. In other words, the melting temperatures of H_2O or H_2 or O_2 likely constrain the lower bound of the solidus/liquidus temperatures (Deemyad & Silvera, 2008; Lin et al., 2005) while those of iron-bearing (e.g., FeO_2, Fe_2O_3) compound likely constrain the upper bound. Here we focus on the upper bound of the solidus/liquidus to examine whether P phase would melt completely near the CMB. The upper limit of calculated congruent melting temperature of the FeO_2 (i.e., LDA or GGA+U) at CMB is ~3,450 K. Assuming a linear relationship between the melting temperature and O content for FeO_x system, the postperovksite phase of Fe_2O_3 melts at 3,350–3,690 K at 136 GPa, which still falls in the lower end of the estimated CMB temperatures (Figure 2).

The incorporation of other elements (e.g., Al, Si, Mg) may also affect melting of P phase. A recent experimental study found that $(Fe,Al)O_2H$ (the solid solution phase of AlO_2H and FeO_2H) is stable at 107–136 GPa and 2,400 K (Zhang et al., 2018). Duan et al. (2018), on the other hand, reported that AlOOH dehydrates at 2,500 K and 142 GPa. As AlO_2H is likely more refractory than FeO_2H (He et al., 2018), the incorporation of Al in P phase may not significantly increase its melting temperature. Also, the amount of AlO_2H phase available at the lowermost mantle is likely very limited (Mashino et al., 2016). In contrast, P phase could be relatively abundant by the reaction of core materials and the water brought by subduction from the crust and the primordial water in the mantle (Hallis et al., 2015; He et al., 2018) proposed by Liu et al. (2017) and Mao et al. (2017). As such, the $(Fe,Al)O_2H$ solid solution at CMB may be very diluted in AlO_2H component and the melting temperature would not be very different from pure P phase discussed above. In addition to Al, dissolving other elements such as Mg and Si may also influence the melting temperature of P phase. However, given the well-known relatively low dehydration temperatures of Mg- and Si-rich hydrous silicate in the lower mantle (Nishi et al., 2014; Ohira et al., 2014), Mg and Si may not significantly affect the melting temperatures of P phase. In addition, whether or not the dissolution of Mg and Si in P phase are energetically favorable needs to be investigated.

To sum up, the solid P phase is likely to melt (completely) in the lowermost mantle even if the P phase melts incongruently or if P phase forms solid solution with AlO_2H. Consequently, P phase cannot be the source of ULVZs.

3.2. Equation of State of FeO_2H_x Solid and Melt

We present the FPMD results on the equation of state and thermodynamic properties mainly focusing on the effects of hydrogen at high pressures. P phase was simulated at 300, 1,000, 2,000, and 3,000 K. Its *P-V* results at 300 K are fit to a third-order Birch-Murnaghan equation of state to obtain K_0 and K' with the reference volume and pressure fixed at the largest volume simulated (Birch, 1978). To represent the *P-V* data at elevated temperatures, we calculate the reference bulk modulus (K_{0T}) at the corresponding temperatures by

$$K_{0T} = K_0 + (\partial K/\partial T)_{0P}(T-300) \quad (1)$$

where $(\partial K/\partial T)_{0P}$ is the temperature derivative of the bulk modulus at the reference pressure. The reference volume (V_{0T}) at evaluated temperatures is expressed as

Table 1
Fitted Equation of State Parameters for P Phase, Liquid FeO_2, FeO_2H, and FeO_2H_5

	V_0 (Å^3)	P_0 (GPa)	T_0 (K)	K_0 (GPa)	K'	K'' (1/GPa)	α_0 (10^{-6} K) or a	α_1 (10^{-9} K^2) or b	$(\partial K/\partial T)_{0P}$ (GPa/K) or c
Solid FeO_2H	22.85	63.8 (0.1)	300	545 (9)	3.0 (0.2)	n.a.	8.9 (0.5)	7.4 (0.4)	−0.041 (0.001)
Liquid FeO_2H	40.69	6.1 (0.1)	3000	26 (4)	7.7 (0.2)	−0.71 (0.05)	22.2 (0.2)	25.5 (0.7)	5.9 (0.4)
Liquid FeO_2	29.44	23 (0.1)	4000	92 (1)	7.1 (0.1)	−0.1605 (0.0004)	n.a.	n.a.	n.a.
Liquid FeO_2H_5	45.15	33.5 (0.1)	4000	136 (5)	2.7 (0.3)	−0.0079 (0.0003)	n.a.	n.a.	n.a.

Uncertainties are given in parentheses. Parameters a, b, and c are dimensionless for the equation of state of liquid (equation (5)). n.a. means not applicable.

$$V_{0T} = V_0 \int_{300}^{T} \alpha_T dT \tag{2}$$

where α_T is the thermal expansion coefficient at high temperatures and the reference pressure and can be further written as

$$\alpha_T = \alpha_0 + \alpha_1 T \tag{3}$$

where α_0 and α_1 are the constants. The fitted parameters are summarized in the Table 1 and the results are plotted in Figure 3a.

Our 300-K isotherm calculated using GGA slightly lies above the high-pressure data (Nishi et al., 2017) and the deviation of volume is within ~0.5%. The experimental values seem to fall into two groups, the low-pressure group (<90 GPa) and high-pressure group (>90 GPa). Similar trend can also be identified in a more recent experimental study (Yuan et al., 2018). We speculate that the dichotomy comes from the dehydrogenation of FeO_2H at high pressure. This speculation is supported by both experimental observations and calculations which show that FeO_2H_x ($x < 1$) is more stable at elevated pressure and temperatures (e.g., He et al., 2018; Yuan et al., 2018). This also explains why most of the first-principles studies "overestimate" volume compared with the high-pressure data by Nishi et al. (2017) (see Figure S4). On the other hand, even if no dehydrogenation occurs in the experiments of Nishi et al. (2017), the isothermal bulk modulus K_T derived by fitting the experimental data directly does not differ much from our results. Within the thermal

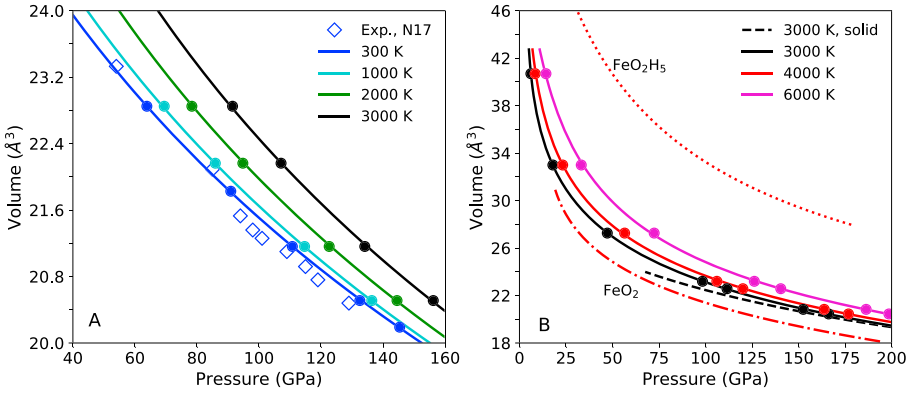

Figure 3. (a) Pressure-volume results of solid P phase at several temperatures (solid lines and solid circles), compared with experimental data at 300 K (open diamonds, N17; Nishi et al., 2017). (b) Pressure-volume results of FeO_2H liquid at 3,000, 4,000, and 6,000 K (solid curves with circles). The equation of state of solid FeO_2H at 3,000 K is shown for comparison (black dashed). Also shown are the calculated results at 4,000 K for liquid FeO_2 (dotted dashed curve) and FeO_2H_5 (dotted curve).

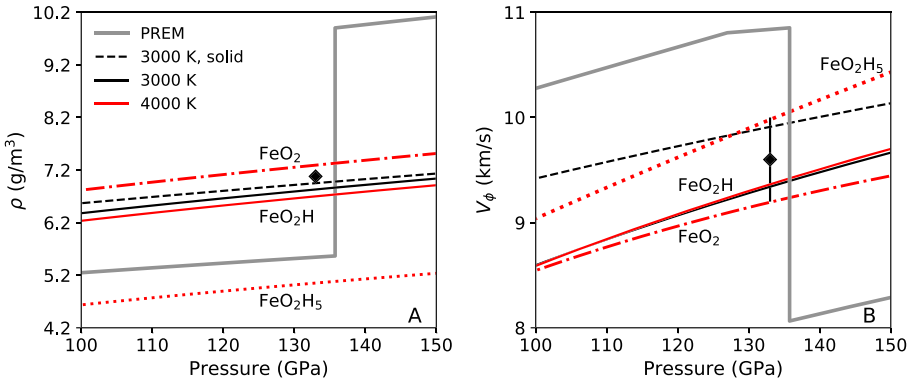

Figure 4. (a) Density and (b) bulk sound velocity of FeO_2H melt at 3,000 and 4,000 K (solid curves), and P phase at 3,000 K (dashed line). The results for FeO_2 and FeO_2H_5 liquids are at 4,000 K. Density and bulk sound velocity of PREM model (Dziewonski & Anderson, 1981) and experimental data (diamond) on the bulk sound velocity of FeO_2H_x at ~2,600 K (Liu et al., 2017) are plotted for comparison. Legend is the same for (a) and (b).

boundary layer (120 to 136 GPa according to Anderson (2002)), the maximum difference in K_T is 2.5%, which corresponds to the difference in bulk sound velocity of 1.2% assuming that the density is the same. Such a small difference is insignificant for this study as shown in the following text.

As for the comparison with other calculations, our 300-K isotherm calculated using GGA almost overlaps with the two lowest-pressure experimental data points on FeO_2H (Lu & Chen, 2018). The differences between GGA and GGA+U results are small (<1%) in the pressure range considered here (Figure S4). While GGA may not produce the correct electronic band gap (Jang et al., 2017; Streltsov et al., 2017), it produces the pressure-volume results, which are comparable to computationally more costly GGA+U results. Moreover, appropriate choice of U and J parameters is not clear. Therefore, we used GGA to calculate the isotherms of P phase and its liquid state.

For liquid FeO_2H_x, x can span from 0 to values greater than 1. x greater than 1 is possible only if the ambient mantle is enriched with hydrogen when melting occurs. Here we consider $x = 0$, 1, and 5, corresponding to hydrogen-depleted to hydrogen-enriched conditions. Liquid FeO_2H was simulated at 3,000, 4,000, and 6,000 K, whereas simulations for liquid FeO_2 and FeO_2H_5 were performed at 4,000 K (Figure 3b). The *P-V-T* results are described to the following expression (Karki et al., 2018):

$$P(V,T) = P(V,T_0) + B_{TH}(T-T_0) \tag{4}$$

Here $P(V, T_0)$ represents the reference isotherm corresponding T_0 taken to be 3,000 K, using a fourth-order Birch-Murnaghan equation of state, and B_{TH} is defined as

$$B_{TH}(V) = \left[a - b\left(\frac{V}{V_0}\right) + c\left(\frac{V}{V_0}\right)^2\right]/1,000 \tag{5}$$

where a, b, and c are the constants. The fitted parameters are summarized in Table 1.

The FPMD results show that both the temperature and hydrogen content increase the volume of liquid FeO_2H_x. The latter has much larger effects. Compared with solid FeO_2H, liquid FeO_2H is less dense for the entire pressure and temperature range considered (Figure 4a), as one would intuitively expect.

Using the pressure-volume-temperature-energy relationships obtained from the FPMD simulations, we can calculate the heat capacity at constant volume (C_V), thermal Gruneisen parameter (γ), and thermal expansivity (α) for both solid and liquid FeO_2H (Figure S5). Both liquid and solid FeO_2H display C_V larger than the Dulong–Petit limit (Figure S5a). Parameter γ of liquid FeO_2H gradually increases with pressure while γ of solid FeO_2H stays nearly constant at the pressures considered here (Figure S5b). Liquid FeO_2H as expected has larger thermal expansion coefficient than its solid counterpart (Figure S5c).

The values of α and γ are necessary to calculate the adiabatic bulk modulus (K_S) from the isothermal bulk modulus (K_T), which can be readily evaluated with $K_T = -(\partial P/\partial \ln V)_T$. At lowermost mantle conditions, α and γ of both liquid and solid FeO_2H vary marginally (Figures S5b and S5c). We thus choose $\alpha = 2 \times 10^{-5}$ K, $\gamma = 1.7$ for liquid FeO_2H and $\alpha = 1.5 \times 10^{-5}$ K, $\gamma = 1.8$ for solid FeO_2H to calculate K_S around CMB conditions using $K_S = K_T(1+\alpha\gamma T)$. For sake of simplicity, we also assume that liquid FeO_2 and FeO_2H_5 have the same α and γ as FeO_2H. Furthermore, the bulk sound velocity (V_ϕ) can be evaluated by $V_\phi = \sqrt{K_s/\rho}$, where ρ is the density (Figure 4b). Our V_ϕ of pyrite-type FeO_2H at 300 and 3,000 K agrees well with Liu et al. (2017) within uncertainties, considering x of 0.5–0.7 in Liu et al. (2017). An increase in x has been suggested to increase the sound velocity of P phase (Huang et al., 2018; Liu et al., 2017). Similar to density, the sound velocity of liquid FeO_2H is much lower than that of its solid counterpart. The sound velocity of liquid FeO_2H_x also strongly depends on the hydrogen content (Figure 4a).

4. Implications for ULVZs

Our first principles results suggest that P phase is unlikely to be the source material of ULVZs based on its relatively low melting temperature. However, liquid FeO_2H_x may be a potential provenance of ULVZs. First, liquid FeO_2H_x is characterized with very low seismic velocity. Its V_ϕ is much lower than the velocity of the isochemical solid and the ambient mantle (Figure 4b). As a result, assuming the *Voigt* average, a mixture of ~20% (by volume) liquid FeO_2H and the ambient mantle can reproduce the seismic observations in ULVZs, while for pyrite-type FeO_2H ~60%–70% of P phase is required (Huang et al., 2018). Given that FeO_2H_x is a minor mineral in the subducted slabs and also may be partly consumed during the course of subduction by reacting with other volatiles such as CO_2 (Boulard et al., 2018), a smaller demand on the amount of delivered FeO_2H_x favors the hypothesis of FeO_2H_x-induced ULVZs. The 20% liquid FeO_2H within the ULVZs could be generated by the reaction of the unlimited iron reservoir in the core and the water brought by subduction from the crust and the primordial water in the mantle (Hallis et al., 2015; He et al., 2018) as originally proposed (Liu et al., 2017; Mao et al., 2017). Second, liquid FeO_2H_x could be maintained in the ambient mantle without drainage. The density of liquid FeO_2H_x is very sensitive to the hydrogen content (Figure 4a). A linear interpolation shows that liquid FeO_2H_x could be neutrally buoyant if x = ~3; that is, FeO_2H_x contains ~3.3 wt % hydrogen. In this case, liquid FeO_2H_x could mix with the ambient mantle free of gravitational separation.

However, such a large amount of H is difficult to justify, since P phase tends to release hydrogen at elevated temperatures (Liu et al., 2017; Yuan et al., 2018). For $0 \le x < 1$, the FeO_2 melt is quite dense (Figure 4a), but the melt viscosity is likely to be negligibly small compared with solid ambient mantle (Karki & Stixrude, 2010). To maintain such a dense melt within the solid mixture against compaction is difficult (Karato, 2014). Yet this is still achievable provided that the topography of the ULVZ region is maintained by the pressure gradient caused by the convective current above that region, as proposed by Hernlund and Jellinek (2010). The degree to which convective stirring keeps melt in a layer can be evaluated by a nondimensional ability parameter, $R = \Delta\rho g H^2/\eta v$, where $\Delta\rho$ is the density difference between the melt and solid matrix; η is the viscosity of the solid matrix; and H, η, and v are the height, viscosity, and convective velocity of ULVZ, respectively (Hernlund & Jellinek, 2010; Jellinek & Manga, 2004). If $R \ll 1$, convective stirring dominates and a substantial amount of melt could be maintained in a layer. Assuming $H = 10$ km (the typical thickness of a ULVZ; Bower et al., 2011) and the solid matrix is composed of the same material as the ambient mantle, R as a function η and v is estimated (Figure 5a) for two different $\Delta\rho$, that is, the density differences between FeO_2 or FeO_2H and the ambient mantle. The ability for a convective pressure gradient to stir melt (R) critically hinges on η and v and is relatively insensitive to the density of liquid itself. Unfortunately, η and v of solid matrix of ULVZs are not well constrained. The estimates of η range from 10^{18} to 10^{21} Pa/s (Forte et al., 2015; Nakada & Karato, 2012). The typical mantle convection rate is 10^{-9} m/s. If the material circulation rate within the ULVZs is of the same order of this value, stirring is unlikely even if the viscosity is 10^{21} Pa/s, unless the ULVZs are very thin (<6 km; Figure 5b). However, near the ULVZ region where a large density anomaly likely exists, much larger velocities may be possible (Karato, 2014). In this case, dense FeO_2H_x melt may be kept within the ULVZs.

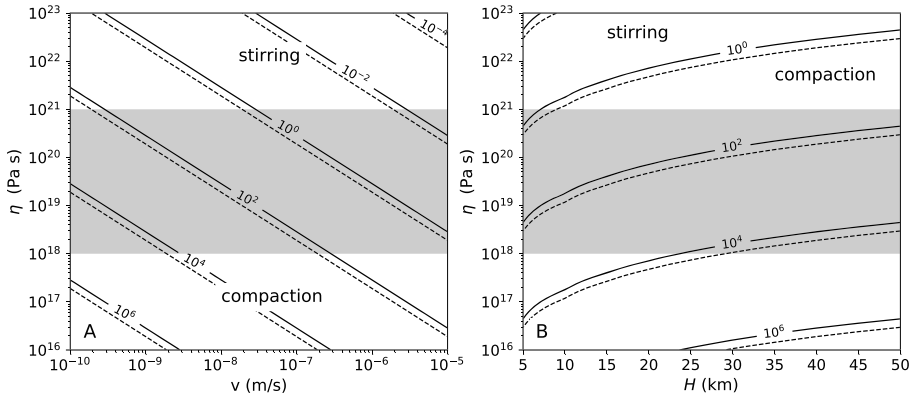

Figure 5. The ability factor (R) for a convective pressure gradient to stir melt to maintain a ULVZ dynamically stable. (a) R as function of the viscosity of the solid matrix (η) and the convecting rate of ULVZs materials (v) for two different melts, FeO_2 (solid contours) and FeO_2H (dashed contours), assuming that the thickness of the ULVZ (H) is 10 km. (b) R as function of the viscosity of the solid matrix (η) and the thickness of ULVZs at a typical convecting rate of ULVZ materials ($v = 10^{-9}$ m/s). $R = 1$ divides the parameter space into two regions, that is, compaction dominant ($R > 1$) and stirring dominant ($R < 1$). The shaded bar represents the literature values of mantle viscosity near CMB (Forte et al., 2015; Nakada & Karato, 2012).

5. Conclusions

We estimated the congruent melting temperatures of both pyrite-type FeO_2H and FeO_2 using first-principles molecular dynamics method. Our results suggest that P phase, whether it is brought down in to the deep mantle by subducted slabs or formed in the lowermost mantle in some other way (Mao et al., 2017), is likely to melt and remain molten near the CMB where ULVZs are located. Our results also suggest that the sound velocity of liquid FeO_2H is much lower than the pyrite-type FeO_2H at the same conditions, thus requiring smaller amounts of FeO_2H liquid to induce the same amount of seismic reduction in ULVZs.

If a ULVZ is indeed composed of a FeO_2H_x melt-bearing slurry, it would be melt-enriched near the top relative to the bottom (Hernlund & Jellinek, 2010) and consequently exhibits the positive gradient in seismic shear velocities, consistent with seismic observations (Rost et al., 2006). However, it requires certain special physical conditions in order to maintain such slurry against compaction. Specifically, these conditions are that hydrogen is extremely enriched (x = ~3) in the melt, or if x is small ($x \ll 3$) the viscosity of the surrounding solid matrix is very viscous and/or ULVZs convect much more vigorously compared with the rest of the mantle.

Acknowledgments
We thank Felipe González-Cataldo and Qijun Hong for the discussions. We are grateful to the three anonymous reviewers for very useful comments and suggestions that improved the manuscript. The research is supported by NSF grants to K.K.M. Lee (EAR-1321956 and EAR-1551348) and B.B. Karki (EAR 1764140). We thank the Yale Center for Research Computing for the guidance and use of the research computing infrastructure, specifically Kaylea Nelson. High-performance computing resources were also provided by Louisiana State University. The thermodynamic data presented in this study can be derived from our equation of state. The data used are listed in the references, figures, and tables.

References

Anderson, O. (1982). The Earth's core and the phase-diagram of iron. *Philosophical Transactions of the Royal Society A-Mathematical Physical and Engineering Sciences*, *45*(11), 1235–1248. https://doi.org/10.5636/jgg.45.1235

Anderson, O. (2002). The power balance at the core–mantle boundary. *Physics of the Earth and Planetary Interiors*, *131*(1), 1–17. https://doi.org/10.1016/S0031-9201(02)00009-2

Andrault, D., Monteux, J., Le Bars, M., & Samuel, H. (2016). The deep Earth may not be cooling down. *Earth and Planetary Science Letters*, *443*, 195–203. https://doi.org/10.1016/j.epsl.2016.03.020

Anzellini, S., Dewaele, A., Mezouar, M., Loubeyre, P., & Morard, G. (2013). Melting of iron at Earth's inner core boundary based on fast X-ray diffraction. *Science*, *340*(6131), 464–466. https://doi.org/10.1126/science.1233514

Belonoshko, A. B., & Rosengren, A. (2012). High-pressure melting curve of platinum from ab initio *Z* method. *Physical Review B*, *85*(17), 174104. https://doi.org/10.1103/PhysRevB.85.174104

Belonoshko, A. B., Skorodumova, N. V., Rosengren, A., & Johansson, B. (2006). Melting and critical superheating. *Physical Review B*, *73*(1), 012201. https://doi.org/10.1103/PhysRevB.73.012201

Birch, F. (1978). Finite strain isotherm and velocities for single-crystal and polycrystalline NaCl at high pressures and 300°K. *Journal of Geophysical Research*, *83*(B3), 1257–1268. https://doi.org/10.1029/JB083iB03p01257

Blöchl, P. E., Jepsen, O., & Andersen, O. K. (1994). Improved tetrahedron method for Brillouin-zone integrations. *Physical Review B*, *49*(23), 16,223–16,233. https://doi.org/10.1103/PhysRevB.49.16223

Boulard, E., Guyot, F., Menguy, N., Corgne, A., Auzende, A.-L., Perrillat, J.-P., & Fiquet, G. (2018). CO_2-induced destabilization of pyrite-structured FeO_2H_x in the lower mantle. *National Science Review*, *5*(6), 870–877. https://doi.org/10.1093/nsr/nwy032

Bower, D. J., Wicks, J. K., Gurnis, M., & Jackson, J. M. (2011). A geodynamic and mineral physics model of a solid-state ultralow-velocity zone. *Earth and Planetary Science Letters*, *303*(3-4), 193–202. https://doi.org/10.1016/j.epsl.2010.12.035

Brown, J., & Shankland, T. J. (1981). Thermodynamic parameters in the Earth as determined from seismic profiles. *Geophysical Journal of the Royal Astronomical Society*, *66*(3), 579–596. https://doi.org/10.1111/j.1365-246X.1981.tb04891.x

Brown, S., Thorne, M. S., Miyagi, L., & Rost, S. (2015). A compositional origin to ultralow-velocity zones. *Geophysical Research Letters*, *42*, 1039–1045. https://doi.org/10.1002/2014GL062097

Deemyad, S., & Silvera, I. F. (2008). Melting line of hydrogen at high pressures. *Physical Review Letters*, *100*(15), 155701. https://doi.org/10.1103/PhysRevLett.100.155701

Deng, J., Du, Z., Benedetti, L. R., & Lee, K. K. M. (2017). The influence of wavelength-dependent absorption and temperature gradients on temperature determination in laser-heated diamond-anvil cells. *Journal of Applied Physics*, *121*(2), 025901. https://doi.org/10.1063/1.4973344

Duan, Y., Sun, N., Wang, S., Li, X., Guo, X., Ni, H., et al. (2018). Phase stability and thermal equation of state of δ-AlOOH: Implication for water transportation to the Deep Lower Mantle. *Earth and Planetary Science Letters*, *494*, 92–98. https://doi.org/10.1016/j.epsl.2018.05.003

Dziewonski, A. M., & Anderson, D. L. (1981). Preliminary reference Earth model. *Physics of the Earth and Planetary Interiors*, *25*(4), 297–356. https://doi.org/10.1016/0031-9201(81)90046-7

Fischer, R. A., & Campbell, A. J. (2010). High-pressure melting of wüstite. *American Mineralogist*, *95*(10), 1473–1477. https://doi.org/10.2138/am.2010.3463

Forte, A. M., Simmons, N. A., & Grand, S. P. (2015). 1.27—Constraints on seismic models from other disciplines—Constraints on 3-D seismic models from global geodynamic observables: Implications for the global mantle convective flow A2 - Schubert, Gerald. In *Treatise on Geophysics*, (Second ed. pp. 853–907). Oxford: Elsevier. https://doi.org/10.1016/B978-0-444-53802-4.00028-2

Ghosh, D. B., & Karki, B. B. (2016). Solid-liquid density and spin crossovers in (Mg, Fe)O system at deep mantle conditions. *Scientific Reports*, *6*(1), 37269. https://doi.org/10.1038/srep37269

González-Cataldo, F., Davis, S., & Gutiérrez, G. (2016). Melting curve of SiO_2 at multimegabar pressures: Implications for gas giants and super-Earths. *Scientific Reports*, *6*(1). https://doi.org/10.1038/srep26537

Hallis, L. J., Huss, G. R., Nagashima, K., Taylor, G. J., Halldórsson, S. A., Hilton, D. R., et al. (2015). Evidence for primordial water in Earth's deep mantle. *Science*, *350*(6262), 795–797. https://doi.org/10.1126/science.aac4834

He, Y., Kim, D. Y., Pickard, C. J., Needs, R. J., Hu, Q., & Mao, H.-k. (2018). Superionic hydrogen in Earth's deep interior. arXiv e-prints. Retrieved from https://ui.adsabs.harvard.edu/\#abs/2018arXiv181008766H

Hernlund, J. W., & Jellinek, A. M. (2010). Dynamics and structure of a stirred partially molten ultralow-velocity zone. *Earth and Planetary Science Letters*, *296*(1-2), 1–8. https://doi.org/10.1016/j.epsl.2010.04.027

Hu, Q., Kim, D. Y., Liu, J., Meng, Y., Yang, L., Zhang, D., et al. (2017). Dehydrogenation of goethite in Earth's deep lower mantle. *Proceedings of the National Academy of Sciences of the United States of America*, *114*(7), 1498–1501. https://doi.org/10.1073/pnas.1620644114

Huang, S., Qin, S., & Wu, X. (2018). Elasticity and anisotropy of the pyrite-type FeO_2H-FeO_2 system in Earth's lowermost mantle. *Journal of Earth Science*. https://doi.org/10.1007/s12583-018-0836-y

Jang, B. G., Kim, D. Y., & Shim, J. H. (2017). Metal-insulator transition and the role of electron correlation in FeO_2. *Physical Review B*, *95*(7), 075144. https://doi.org/10.1103/PhysRevB.95.075144

Jellinek, A. M., & Manga, M. (2004). Links between long-lived hot spots, mantle plumes, *D″*, and plate tectonics. *Reviews of Geophysics*, *42*, RG3002. https://doi.org/10.1029/2003RG000144

Karato, S.-I. (2014). Does partial melting explain geophysical anomalies? *Physics of the Earth and Planetary Interiors*, *228*, 300–306. https://doi.org/10.1016/j.pepi.2013.08.006

Karki, B. B., Ghosh, D. B., Maharjan, C., Karato, S.-I., & Park, J. (2018). Density-pressure profiles of Fe-bearing $MgSiO_3$ liquid: Effects of valence and spin states, and implications for the chemical evolution of the lower mantle. *Geophysical Research Letters*, *45*, 3959–3966. https://doi.org/10.1029/2018GL077149

Karki, B. B., & Stixrude, L. P. (2010). Viscosity of $MgSiO_3$ liquid at Earth's mantle conditions: Implications for an early magma ocean. *Science*, *328*(5979), 740–742. https://doi.org/10.1126/science.1188327

Kresse, G., & Joubert, D. (1999). From ultrasoft pseudopotentials to the projector augmented-wave method. *Physical Review B*, *59*(3), 1758–1775. https://doi.org/10.1103/PhysRevB.59.1758

Li, D., Zhang, P., & Yan, J. (2014). Ab initio molecular dynamics study of high-pressure melting of beryllium oxide. *Scientific Reports*, *4*(1), 4707. https://doi.org/10.1038/srep04707

Lin, J.-F., Gregoryanz, E., Struzhkin, V. V., Somayazulu, M., Mao, H.-k., & Hemley, R. J. (2005). Melting behavior of H_2O at high pressures and temperatures. *Geophysical Research Letters*, *32*, L11306. https://doi.org/10.1029/2005GL022499

Liu, J., Hu, Q., Young Kim, D., Wu, Z., Wang, W., Xiao, Y., et al. (2017). Hydrogen-bearing iron peroxide and the origin of ultralow-velocity zones. *Nature*, *551*(7681), 494–497. https://doi.org/10.1038/nature24461

Lu, C., & Chen, C. (2018). High-pressure evolution of crystal bonding structures and properties of FeOOH. *The Journal of Physical Chemistry Letters*, *9*(9), 2181–2185. https://doi.org/10.1021/acs.jpclett.8b00947

Mao, H.-K., Hu, Q., Yang, L., Liu, J., Kim, D. Y., Meng, Y., et al. (2017). When water meets iron at Earth's core–mantle boundary. *National Science Review*, *4*(6), 870–878. https://doi.org/10.1093/nsr/nwx109

Mao, W. L., Mao, H.-k., Sturhahn, W., Zhao, J., Prakapenka, V. B., Meng, Y., et al. (2006). Iron-rich post-perovskite and the origin of ultralow-velocity zones. *Science*, *312*(5773), 564–565. https://doi.org/10.1126/science.1123442

Mashino, I., Murakami, M., & Ohtani, E. (2016). Sound velocities of δ-AlOOH up to core-mantle boundary pressures with implications for the seismic anomalies in the deep mantle. *Journal of Geophysical Research: Solid Earth*, *121*, 595–609. https://doi.org/10.1002/2015JB012477

Morard, G., Andrault, D., Antonangeli, D., Nakajima, Y., Auzende, A. L., Boulard, E., et al. (2017). Fe–FeO and Fe–Fe_3C melting relations at Earth's core–mantle boundary conditions: Implications for a volatile-rich or oxygen-rich core. *Earth and Planetary Science Letters*, *473*, 94–103. https://doi.org/10.1016/j.epsl.2017.05.024

Nakada, M., & Karato, S. (2012). Low viscosity of the bottom of the Earth's mantle inferred from the analysis of Chandler wobble and tidal deformation. *Physics of the Earth and Planetary Interiors*, *192-193*, 68–80. https://doi.org/10.1016/J.Pepi.2011.10.001

Nishi, M., Irifune, T., Tsuchiya, J., Tange, Y., Nishihara, Y., Fujino, K., & Higo, Y. (2014). Stability of hydrous silicate at high pressures and water transport to the deep lower mantle. *Nature Geoscience*, *7*(3), 224–227. https://doi.org/10.1038/ngeo2074

Nishi, M., Kuwayama, Y., Tsuchiya, J., & Tsuchiya, T. (2017). The pyrite-type high-pressure form of FeOOH. *Nature*, *547*(7662), 205–208. https://doi.org/10.1038/nature22823

Nomura, R., Hirose, K., Uesugi, K., Ohishi, Y., Tsuchiyama, A., Miyake, A., & Ueno, Y. (2014). Low core-mantle boundary temperature inferred from the solidus of pyrolite. *Science*, *343*(6170), 522–525. https://doi.org/10.1126/science.1248186

Nomura, R., Ozawa, H., Tateno, S., Hirose, K., Hernlund, J., Muto, S., et al. (2011). Spin crossover and iron-rich silicate melt in the Earth/'s deep mantle. *Nature*, *473*(7346), 199–202. https://doi.org/10.1038/nature09940

Ohira, I., Ohtani, E., Sakai, T., Miyahara, M., Hirao, N., Ohishi, Y., & Nishijima, M. (2014). Stability of a hydrous δ-phase, AlOOH–$MgSiO_2(OH)_2$, and a mechanism for water transport into the base of lower mantle. *Earth and Planetary Science Letters*, *401*, 12–17. https://doi.org/10.1016/j.epsl.2014.05.059

Perdew, J. P., Burke, K., & Ernzerhof, M. (1996). Generalized gradient approximation made simple. *Physical Review Letters*, *77*(18), 3865–3868. https://doi.org/10.1103/PhysRevLett.77.3865

Rost, S., Garnero, E. J., & Williams, Q. (2006). Fine-scale ultralow-velocity zone structure from high-frequency seismic array data. *Journal of Geophysical Research*, 111, B09310. https://doi.org/10.1029/2005JB004088

Seagle, C. T., Heinz, D. L., Campbell, A. J., Prakapenka, V. B., & Wanless, S. T. (2008). Melting and thermal expansion in the Fe–FeO system at high pressure. *Earth and Planetary Science Letters*, *265*(3–4), 655–665. https://doi.org/10.1016/j.epsl.2007.11.004

Streltsov, S. S., Shorikov, A. O., Skornyakov, S. L., Poteryaev, A. I., & Khomskii, D. I. (2017). Unexpected 3+ valence of iron in FeO_2, a geologically important material lying "in between" oxides and peroxides. *Scientific Reports*, *7*(1), 13005. https://doi.org/10.1038/s41598-017-13312-4

Tang, M., Niu, Z.-W., Zhang, X.-L., & Cai, L.-C. (2018). Structural stability of FeO_2 in the pressure range of lower mantle. *Journal of Alloys and Compounds*, *765*, 271–277. https://doi.org/10.1016/j.jallcom.2018.06.237

Wang, S., Zhang, G., Liu, H., & Song, H. (2013). Modified *Z* method to calculate melting curve by molecular dynamics. *The Journal of Chemical Physics*, *138*(13), 134101. https://doi.org/10.1063/1.4798225

Wicks, J. K., Jackson, J. M., & Sturhahn, W. (2010). Very low sound velocities in iron-rich (Mg,Fe)O: Implications for the core-mantle boundary region. *Geophysical Research Letters*, *37*, L15304. https://doi.org/10.1029/2010GL043689

Williams, Q., & Garnero, E. J. (1996). Seismic evidence for partial melt at the base of Earth's mantle. *Science*, *273*(5281), 1528–1530. https://doi.org/10.1126/science.273.5281.1528

Yuan, L., Ohtani, E., Ikuta, D., Kamada, S., Tsuchiya, J., Naohisa, H., et al. (2018). Chemical reactions between Fe and H_2O up to megabar pressures and implications for water storage in the Earth's mantle and core. *Geophysical Research Letters*, *45*, 1330–1338. https://doi.org/10.1002/2017GL075720

Zhang, L., Yuan, H., Meng, Y., & Mao, H.-k. (2018). Discovery of a hexagonal ultradense hydrous phase in (Fe,Al)OOH. *Proceedings of the National Academy of Sciences of the United States of America*, *115*(12), 2908–2911. https://doi.org/10.1073/pnas.1720510115

Zhang, X.-L., Niu, Z.-W., Tang, M., Zhao, J.-Z., & Cai, L.-C. (2017). First-principles thermoelasticity and stability of pyrite-type FeO_2 under high pressure and temperature. *Journal of Alloys and Compounds*, *719*, 42–46. https://doi.org/10.1016/j.jallcom.2017.05.143